Food and Chemical Toxicology 128 (2019) 81–88

Contents lists available at ScienceDirect

Food and Chemical Toxicology

journal homepage: www.elsevier.com/locate/foodchemtox

# Insight into the formation, structure and digestibility of lotus seed amylose-fatty acid complexes prepared by high hydrostatic pressure

Zebin Guo[a,b,c], Xiangze Jia[a,b,c], Xiong Lin[a,b,c], Bingyan Chen[a,b,c], Siwei Sun[a,b,c], Baodong Zheng[a,b,c,*]

[a] College of Food Science, Fujian Agriculture and Forestry University, Fuzhou, Fujian, PR China
[b] Fujian Provincial Key Laboratory of Quality Science and Processing Technology in Special Starch, Fuzhou, Fujian, PR China
[c] China-Ireland International Cooperation Centre for Food Material Science and Structure Design, Fujian Agriculture and Forestry University, Fuzhou, PR China

ARTICLE INFO

*Keywords:*
High hydrostatic pressure
Lotus seed amylose-fatty acid complex
Structure
Digestibility

ABSTRACT

Lotus seed amylose-fatty acid complexes were prepared using high hydrostatic pressure and the relationship between their structural properties and digestibility was investigated. The formation of lotus seed amylose-fatty acid complexes increased the values of weight molar mass (*Mw*), number molar mass (*Mn*), polydispersity index and resistant starch content compared to those of amylose controls. *Mw* and *Mn* values of lotus seed amylose and complexes decreased with an increase in high hydrostatic pressure from 500 MPa to 600 MPa, suggesting that the lotus seed amylose was decomposed into short glucan chains. The presence of single helical lotus seed amylose-fatty acid complexes and double helical retrograded amylose was investigated using Raman spectroscopy and imaging. The results from Raman spectra and *in vitro* digestion showed that the content of both single helical LSA-fatty acid complexes and double helical retrograded LSA were responsible for digestibility of the complex matrix.

## 1. Introduction

Growing evidence shows that many chronic diseases such as obesity, cardiovascular disease and diabetes could be prevented or moderated through a low-calorie intake (Birt et al., 2013). The energy intake from staple foods, precisely prandial starch, contributes more than 90% of the calorie intake in developing countries (Guo et al., 2017). Decreasing the digestibility of starch or directly ingesting resistant starch and other dietary fibers could regulate the glycemic response (Ma and Boye, 2018; Zaman and Sarbini, 2016). Remarkably, resistant starches are merely decomposed in the large intestine and positively promote the proliferation of gut microflora (Guo et al., 2017).

It is crucial to recognize that non-starch food matrix components can influence the structure and digestibility of starch. Evidence has demonstrated that polyphenols (Zhao et al., 2018), hydrogels (Oh et al., 2018), proteins (Chen et al., 2018) and lipids (Farooq et al., 2018) can potentially decrease the digestibility of starch because of the formation of resistant starch or slowly digestible starch. A novel defined resistant starch (type-5), namely amylose-lipid complex, is widely found in processed starchy foods, especially in thermally processed products, which largely contain water, starch and lipids. Amylose within starch granules are expected to be released during food processing which resulting in gelatinization. In thermal liquid conditions, the free linear amylose macromolecules are folded into single-helical conformation with external hydrophilic hydroxyls and an internal hydrophobic cavity (Putseys et al., 2010). This framework is beneficial for attracting the aliphatic chains of lipids into the amylose hydrophobic cavity and forming stable crystal complexes. The small macromolecules of complexes could further aggregate into submicron spherulites, which tend to be more resistant to digestion (Zabar et al., 2010). Besides, the single helical amylose become more susceptible to retrograde as double helix due to the disappearance of ambient forces (Wang et al., 2015).

Non-thermal food processing technologies are of particular interest due to the preferable preservation of thermal-unstable nutrients (Guo et al., 2019). Recent studies have shown that several non-thermal conditions can induce starch gelatinization to different degrees such as pulse electric field, ultrasound, microwave, irradiation and high hydrostatic pressure (HHP) (Zhang et al., 2019). The innovative approach of HHP displays many advantages, including easy manipulation, large handling capacity and high efficiency in food treatments and also in starch non-thermal gelatinization (Yang et al., 2017). This makes it useful as a potential preparation method for resistant starch type-5 (RS5).

Lotus (*Nelumbo nucifera* Gaertn.) seed was recently categorized as dual-purpose resources for food and drugs by the National Health and

* Corresponding author. College of Food Science, Fujian Agriculture and Forestry University, Fuzhou, Fujian, 350002, PR China.
*E-mail address:* zbdfst@yeah.net (B. Zheng).

https://doi.org/10.1016/j.fct.2019.03.052
Received 19 February 2019; Received in revised form 26 March 2019; Accepted 28 March 2019
Available online 02 April 2019

Planning Commission of China. The interactions between lotus seed starch and small ligands, especially lipids occur under practically all processing conditions (Guo et al., 2017). Our previous studies demonstrated that lotus (*Nelumbo nucifera* Gaertn.) seed starch is entirely gelatinized when exposed to 600 MPa HHP treatment (Guo et al., 2015a, 2015b), and lotus seed amylose (LSA) can form complexes with both saturated and unsaturated fatty acids at 500 MPa (Jia et al., 2018). Findings also suggested that the thermal-stable LSA-fatty acid complex contained both V-type crystal single helical complexes and B-type crystal double helical retrograded amylose (Guo et al., 2018). Therefore, this non-thermal produced complex warrants further study to investigate the relationship between macro-molecular conformations and digestibility. In addition, there has been a lack of knowledge about the spectroscopic images of amylose-fatty acid complexes until recently. In order to gain a better understanding on whether the amylose single or double helix affects the formation and digestibility of amylose-fatty acid complexes, Raman spectra and its spectroscopy were employed to examine the conformational changes of free LSA and complexes during HHP treatments. The formation, morphology and digestibility were investigated by complex index (CI), molecular weight distribution, confocal laser scanning microscopy (CLSM), scanning electron microscopy (SEM) and *in vitro* digestion. The work addresses how, after HHP treatment, linear single helix amylose formed complexes with fatty acids or retrograded itself as a double helix, and whether these two components influence the digestibility of the complex matrix.

## 2. Materials and methods

### 2.1. Materials

Lotus seed starch was segregated from frozen lotus seeds (Green Field Fujian Food Co. Ltd., China) on the basis of a previously reported method (Guo et al., 2015a). Peeled lotus seeds and water were crushed in a DS-200 shredder (Changzhou Xiangtian Experimentation Instrument Plant Co. Ltd., China), and the juice was filtered through a 100-mesh sieve. The starch sediment was centrifuged and further washed for three times with distilled water. An 95% ethanol solution (m/v) was utilized to eliminate attached lipids on the lotus seed starch granules. The dried starch was utilized for the extraction of LSA using a repetitive organic-solution method (Guo et al., 2018). Briefly, lotus seed starch was dissolved in a 0.5 mol/L sodium hydroxide (NaOH) hydrothermal solution and stirred intensively for complete separation of LSA. An isopentanol/*n*-butanol solution (33%, v/v) was utilized to settle the crude LSA from the dispersion after neutralization with 2 mol/L chlorine hydride (HCl) solution. LSA precipitate was dissolved and thermally washed for several times with saturated aqueous *n*-butanol solution, and after that purified with pure ethanol. The resulting amylose content of LSA was 88.1 ± 1.5%, as characterized via the Megazyme amylose/amylopectin assay kit (Megazyme, Ireland). The fatty acids, lauric acid (C12:0), myristic acid (C14:0), and palmitic acid (C16:0), were purchased from Macklin Biochemical (Shanghai Macklin Biochemical Co. Ltd., China). Amyloglucosidase from *Aspergillus niger* (100000 U/mL) and α-amylase from the hog pancreas (50 U/mg) were obtained from Macklin Biochemical (Shanghai Macklin Biochemical Co. Ltd., China) and Sigma-Aldrich (Sigma-Aldrich, USA), respectively. A glucose assay kit (GOPOD Format) was purchased from Megazyme (Megazyme, Ireland). All of the other reagents were of analytical grade.

### 2.2. Preparation of LSA-fatty acid complexes by HHP

LSA-fatty acid complexes were prepared based on the method (Guo et al., 2018) with few modification. Briefly, the LSA (5 g) and each fatty acid (0.5 g) were dispersed in 500 ml of 10% (v/v) ethanol solution and then vacuum-packaged in polypropylene bags. The mixture was treated in an HHP system (KeFa High Pressure Technology, China). The samples were disposed to hydrostatic pressures of 500 and 600 MPa in a high-pressure metal vessel at room temperature (25 °C). Additionally, this procedure was performed for 30 min with an accelerating rate of virtually 15 MPa/s. The HHP-treated samples were washed with pure ethanol to remove non-complexed fatty acids, filtered, lyophilized, and then crushed into small particles to pass them through an 80-mesh sieve.

### 2.3. CI value of LSA-fatty acid complexes

The CI value of the complexes were calculated to investigate the extent of complex formation, as presented previously (Jia et al., 2018). 0.3 g of each complex sample was dispersed in 5 mL of distilled water, and the suspension was thermal bathed in boiling water for 20 min. The dispersion was then centrifuged after cooling, and 50 μL of supernatant was mixed with 4 mL of iodine-potassium iodide solution in test tube that was gently vortexed. Absorbance (ABS) values of the complexes and amylose controls were measured at 690 nm with a UV–VIS spectrophotometer. The CI was calculated using the following formulae:

$$CI\,(\%) = 100 \times \frac{ABS_{reference} - ABS_{sample}}{ABS_{reference}} \quad (1)$$

In this equation, $ABS_{reference}$ and $ABS_{sample}$ represent the absorbance value of LSA and complexes, respectively.

### 2.4. CLSM

Approximately 20 mg of each sample was mixed with 1 mL Nile Red fluorescence dye solution (1 g/L in pure methanol) and reacted avoid light for 12 h to label the fatty acid. The centrifuged precipitate was further washed with pure methanol to remove free Nile Red. The sample was examined with a TCS SP8X DLS CLSM (Leica, Germany) which equipped with photomultiplier tubes. The excitation wavelength was 514 nm, and the Leica objective lens was 20×.

### 2.5. SEM

The presence of submicron crystal spherulites indicates the formation of amylose-fatty acid complexes. SEM system was employed to observe the morphology of spherulites within LSA-fatty acid complexes. The lyophilized samples were adhered on an aluminum stub with double-sided conductive adhesive tape and then coated with a 50 nm thickness gold layer. Morphology of samples was investigated by a Nova NanoSEM 230 (FEI, USA) with an accelerating voltage of 5 keV in low vacuum operating mode.

### 2.6. Molecular mass distribution

The molar mass distributions of samples were obtained and analyzed employing high-performance size-exclusion chromatography (HPSEC) which connected with a multi-angle laser light-scattering and refractive index (HPSEC-MALLS-RI) system on the basis of previously reported methods with slight modifications (Guo et al., 2015a). The mobile phase composed of 90% dimethyl sulfoxide solution (DMSO) with lithium bromide (LiBr) (50 mmol/L), filtered through a 0.22 μm PTFE membrane filter and then subjected to ultrasound treatment. For size-exclusion chromatography (SEC) analysis, 12.5 mg sample was dispersed in 5 mL of 50 mmol/L LiBr in DMSO. Dispersed samples were analyzed using an HPSEC system which was equipped with a 12-6 HPLC pump (Wyatt Technology, USA) and an injector with a 1 mL loop. The loop was connected to an 18-angle Dawn-Heleos II MALLS detector (Wyatt Technology, USA), which had a laser wavelength of 664.1 nm, and a Shodex RI-101 refractive index detector (Shodex, Japan). Diluted sample dispersion was filtered and passed through 5 μm Millipore PTFE filter film and then injected with a manual injector directly into a MALLS detector at a flow rate of 0.3 mL/min. The columns used were Ohpak SB-G (Shodex, Japan) and Ohpak SB-806 HQ (Shodex, Japan)

columns, selected in series and maintained at 35 °C. *Mw* and *Mn* were obtained employing the Astra V software (Wyatt Technology, USA) according to the Zimm model.

### 2.7. Raman spectra and spectroscopy

The short-range molecular structure of samples was determined using Raman spectra and spectroscopy. The samples were dispersed in a 70% (v/v) ethanol solution for 24 h. A barium fluoride ($BaF_2$) plate (13 mm × 2 mm) was used to load liquid-state samples and transmit single infrared light. The spectral analysis and imaging of LSA-fatty acid complexes were performed with a DXRxi Raman microscope system (Thermofisher Scientific, USA). The scan range was 600–3300 $cm^{-1}$, imaging area was 50 mm × 50 mm and the resolution ratio was approximately 2 $cm^{-1}$.

### 2.8. In vitro digestion

The *in vitro* digestion of complexes and LSA controls was measured using previously reported procedures (Englyst et al., 1999) (Zhang et al., 2012) with modifications. Samples were dispersed into distilled water and then placed in a boiling water bath for 30 min. Cooled samples were dispersed in sodium acetate buffer with the addition of enzyme solution (sodium phosphate buffer, amyloglucosidase and α-amylase) and further incubated at 37 °C in a water bath. The amount of glucose released from samples at each time point were measured (0, 20, 40, 60, 90, 120, 150 and 180 min) using GOPOD method. The ratio of hydrolyzed starch was calculated using the follow equation:

$$Starch\ \ hydrolysis\ \ (\%) = \frac{TG}{TS} \times \frac{162}{180} \times 100 \quad (2)$$

In this equation, TG was the total mass of glucose released and TS was the total mass of sample. Values of rapidly digestible starch (RDS), slowly digestible starch (SDS), and resistant starch (RS) were calculated from the amounts of glucose released within 20 min ($G_{20}$) and 120 min ($G_{120}$), using the follow equations:

$$\begin{aligned} RDS(\%) &= [(G_{20} - G_0)/TS] \times 0.9 \times 100 \\ SDS(\%) &= [(G_{120} - G_{20})/TS] \times 0.9 \times 100 \\ RS(\%) &= [(TS - G_{120})/TS] \times 0.9 \times 100 \end{aligned} \quad (3)$$

### 2.9. Statistical analysis

Measurements were performed in triplicate for analysis. The variance analysis and mean separations were carried out with Duncan's multiple-range test ($p < 0.05$) using DPS analysis software 9.5 (Science Press, China).

## 3. Results and discussion

### 3.1. Analysis of CI

The CI value indicates the extent of formation of LSA-fatty acid complexes (Annor et al., 2015). The effect of different processing pressures and fatty acids on the CI value of complexes is shown in Fig. 1. In the 500 MPa group, the CI values of complexes were larger in the order of LSA-lauric acid (LSA-C12:0) > LSA-myristic acid (LSA-C14:0) > LSA-palmitic acid (LSA-C16:0). These results correspond with previous work (Kawai et al., 2012); (Tang and Copeland, 2007) which postulated that CI values showed a tendency to increase as the number of carbon atoms in the fatty acid decreased. Fatty acids have low water solubility, and thus have low dispersivity in the mixture. Therefore, it is thought that complex formation between LSA and fatty acids was facilitated by the unwinding of amylose under HHP, which lead to the hydrophobic LSA left-hand cavities (Guo et al., 2018). Thus, the aliphatic chains of saturated fatty acids were entrapped in hydrophobic

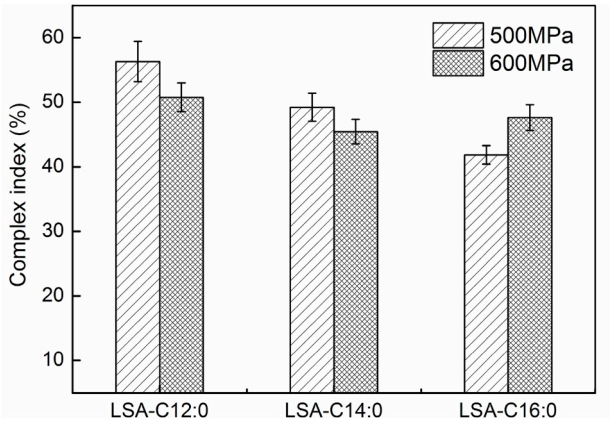


**Fig. 1.** Complex index of samples prepared under different HHPs. The abbreviations LSA, LSA-C12:0, LSA-C14:0, and LSA-C16:0 represent lotus seed amylose, lotus seed amylose–lauric acid, lotus seed amylose–myristic acid, and lotus seed amylose–palmitic acid, respectively.

cavity of LSA. In the 600 MPa group, the CI values of complexes increased in the disordered sequence of LSA-C12:0 > LSA-C16:0 > LSA-C14:0. It was assumed that the high-intensity HHP treatment changes the order structure of starch chain, further impact the complex mechanism with fatty acids. Therefore, for both the 500 MPa and 600 MPa treatments, the complex of LSA-C12:0 exhibited the highest CI value. It is thought that the long chain fatty acids result in poor complex formation with amylose because of their poor dispersivity (Fredrik et al., 2003). Conversely, fatty acids with shorter chains have better capacity to form single-helical complexes with LSA because of their relatively high dispersivity and low steric hindrance.

### 3.2. Morphology of complexes

In the present work, the formation of LSA-fatty acid complexes and their morphology was investigated by CLSM after samples were stained with Nile Red, which forms stable complexes with fatty acids and emits a fluorescent signal under a specific excitation wavelength. The optical sections revealing the distribution of fatty acids within complexes are shown in Fig. 2. In our previous study, lower fluorescence intensities were observed in the LSA controls compared with those of complexes (Jia et al., 2018). Less fluorescence of Nile Red was observed in the LSA control treated with 600 MPa than with 500 MPa, and was due to the loose and porous arrangement, which enabled easy removal of the Nile Red molecule by methanol. The strong fluorescence intensity of complexes indicates the formation of LSA-fatty acid complexes and the bright red spots represent the crystalline free fatty acids entrapped within amylose lamellaes (Marinopoulou et al., 2016). Varying the carbon chain length of fatty acids and processing pressure resulted in no significant differences among any of the complexes.

SEM was employed to observe the microscopic attributes of the complexes. The LSA controls were displayed as irregular fragments. According to previous SEM and wide angle X-ray diffraction studies (Guo et al., 2018; Zeng et al., 2018), these irregular fragments were attributable to B-type retrograded amylose. It has been suggested that the submicron spherulite, consisting of ordered crystal lamellaes, is an indicator of the amylose-fatty acid complex (Zabar et al., 2009). In this study, results indicated that all three fatty acids can form a spheroidal complex with LSA under both 500 MPa and 600 MPa HHP treatments (Fig. 2). Many of the spherulites further aggregated into relatively large particles which potentially contributed to the anti-digestibility due to the ordered crystal structure. In addition, there were no evidently differences in morphology observed between complexes reacting with different fatty acids or under different HHP processing treatments.

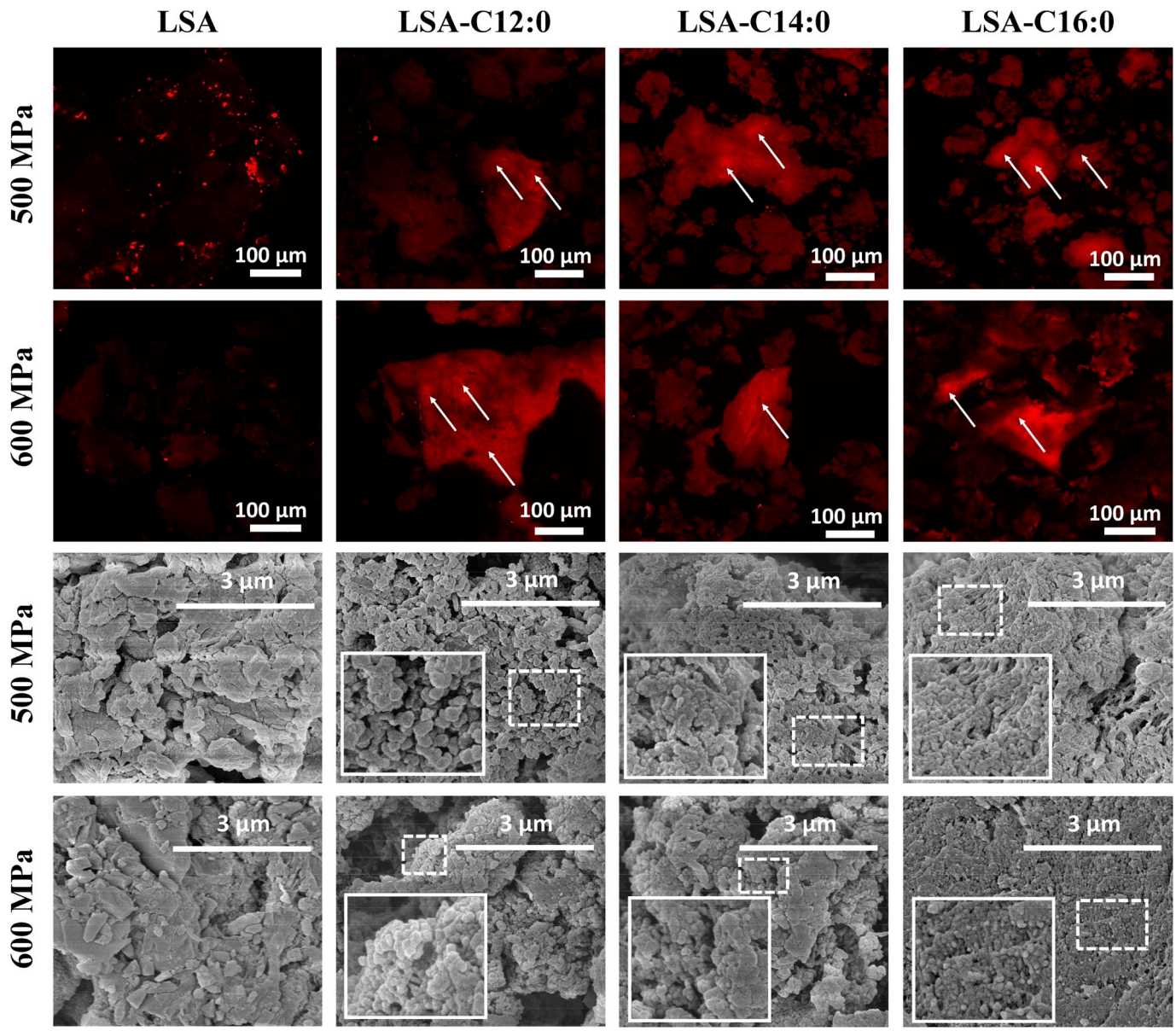


**Fig. 2.** Confocal laser scanning microscopy and scanning electron microscopy of samples prepared under different HHPs. The abbreviations LSA, LSA-C12:0, LSA-C14:0, and LSA-C16:0 represent lotus seed amylose, lotus seed amylose–lauric acid, lotus seed amylose–myristic acid, and lotus seed amylose–palmitic acid complex, respectively. White arrows indicate spots of free entrapped fatty acids. The area within dashed white line is amplified at the lower-left corner of each figure.

### 3.3. Molecular weight distribution

The *Mw*, *Mn* and polydispersity values of LSA controls and complexes are summarized in Table 1. The formation of LSA-fatty acid complexes increased the values of *Mw*, *Mn* and polydispersity for both 500 MPa and 600 MPa treatments, compared to the LSA controls. It has been suggested that fatty acids can form inclusion complexes with linear amylose exhibiting a higher degree of polymerization (Cao et al., 2015). The increase in *Mw* and *Mn* of amylose complexes also indicates that LSA-fatty acid single-helical complexes were stable in the DMSO eluent. The value of polydispersity index represents the different ranges of molecular weight distribution, briefly the larger the polydispersity value of macromolecules, the wider the molecular weight distribution (Yoo and Jane, 2002). In this study, the complexes showed higher polydispersity values compared to LSA, and this phenomenon was associated with the partial reaction between LSA and fatty acids, and in accordance with our previous X-ray diffraction result.

Both *Mw* and *Mn* values of LSA decreased with increasing HHP treatments from 500 MPa to 600 MPa, suggesting that LSA was decomposed and formed glucan chains with a lower degree of polymerization (Guo et al., 2015a), and this further lead to the decline of *Mw* and *Mn* values of complexes.

### 3.4. Analysis of Raman spectra and spectral imaging

In the study of molecular weight distribution of this paper, we found that part of LSA formed a complex with fatty acids. Theoretically, two of the main existing forms of amylose are single helical amylose-fatty acid complex and double-helical retrograded amylose. Here, structural analysis by Raman spectroscopy was carried out to investigate the conformation and short-range ordered molecular structure of LSA within complexes. The Raman spectra of samples are shown in Fig. 3 (A1 and B1). Characteristic bands observed at 865, 943, 1343 and 2900 $cm^{-1}$ are shown in the LSA controls for both 500 MPa and 600 MPa treatments. The complexes, showing several clear bands, could be observed around 865, 943, 1265, 1343 and 2900 $cm^{-1}$ in

**Table 1**
Molecular weight of complexes prepared by lotus seed amylose and fatty acids with different chain length.[a]

| | Sample[b] | *Mw* (kDa) | *Mn* (kDa) | Polydispersity |
|---|---|---|---|---|
| 500 MPa | LSA | 641.0 ± 0.022d | 237.0 ± 0.060c | 2.704 ± 0.064c |
| | LSA-C12:0 | 1184.2 ± 0.017c | 357.9 ± 0.027b | 3.309 ± 0.032 ab |
| | LSA-C14:0 | 1238.9 ± 0.018a | 358.6 ± 0.019b | 3.455 ± 0.027a |
| | LSA-C16:0 | 1193.9 ± 0.013b | 372.4 ± 0.019a | 3.206 ± 0.023b |
| 600 MPa | LSA | 516.2 ± 0.013d | 235.3 ± 0.019d | 2.193 ± 0.002d |
| | LSA-C12:0 | 735.4 ± 0.017c | 242.6 ± 0.035c | 3.031 ± 0.039c |
| | LSA-C14:0 | 983.0 ± 0.015b | 296.1 ± 0.024b | 3.320 ± 0.029b |
| | LSA-C16:0 | 1182.7 ± 0.017a | 329.4 ± 0.020a | 3.591 ± 0.026a |

[a] Data are the averages of three determinations. Values with superscript letters (different samples from the same HHP treatment) within a column are significantly different ($P < 0.05$).
[b] The abbreviations LSA, LSA-C12:0, LSA-C14:0, and LSA-C16:0 represent lotus seed amylose, lotus seed amylose–lauric acid, lotus seed amylose–myristic acid, and lotus seed amylose–palmitic acid, respectively.

Raman spectra, which are related to υs (C1-O-C4), υs (C1-O-C5), δ ($CH_2OH$), δ (C-O-H bending, $CH_2$ twisting) and υ (C-H) modes, respectively (Mutungi et al., 2012; Wang et al., 2018; Xiang et al., 2018). The band at 865 $cm^{-1}$ indicates C1-O-C4 groups in the glucosyl rings, which appear to be aligned roughly along the axis of the amylose double-helix structure. The intense signal of complexes around 1265 $cm^{-1}$ could be attributed to $CH_2OH$-related deformation, and indicates the LSA-fatty acid complexes were of V-type crystals, which further indicates the formation of RS5. The intense characteristic band at 1343 $cm^{-1}$ could be ascribed to the bond angle shift of C-O-H, which was roughly induced by the spiralization of single-helical amylose (Cael et al., 1975; Galvis et al., 2015, 2016; Gonzalez-Cruz et al., 2018; Haaj et al., 2013; Wellner et al., 2011). For both HHP treatments, the intensity of these bands increased in the order of LSA-C12:0 > LSA-C14:0 > LSA-C16:0, indicating that fatty acids with shorter carbon chains exhibit better complexation with LSA under HHP treatments.

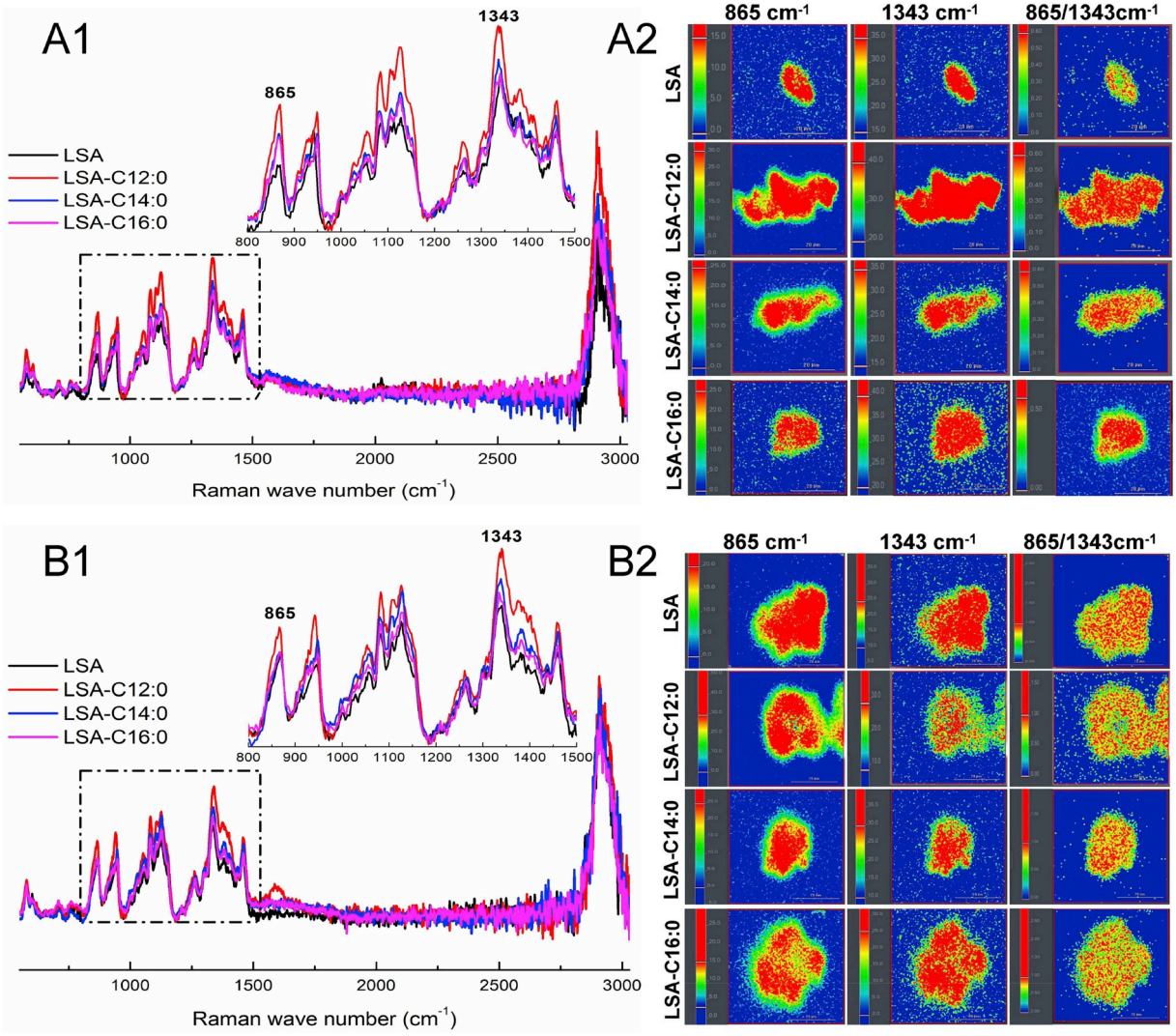


**Fig. 3.** Raman spectra and imaging of samples prepared under different HHPs (A: 500 MPa; B: 600 MPa). The abbreviations LSA, LSA-C12:0, LSA-C14:0, and LSA-C16:0 represent lotus seed amylose, lotus seed amylose–lauric acid, lotus seed amylose–myristic acid, and lotus seed amylose–palmitic acid, respectively.

Furthermore, a slight reduction of intensity peaks at 865 and 1343 $cm^{-1}$ were observed with an increase in HHP processing pressure, which may be attributed to the decomposition of the LSA chain structure induced by higher pressure (Guo et al., 2018).

In order to gain a better understanding of the distribution of single-helical LSA and double-helical retrograded LSA, Raman spectral imaging was performed to investigate the distribution of selected spectroscopic features for amylose and was performed with 2D Raman intensity imaging. Fig. 3 (A2 and B2) shows Raman images calculated from the measured intensities at bands of 865, 1343 and 865/1343 $cm^{-1}$. The color scale from blue to red was selected to emphasize an increase in the level of different amylose conformations across the samples. Intensities at 865 and 1343 $cm^{-1}$ represented the double-helical retrograded LSA and single-helical LSA, respectively, and the image measured at 856/1343 $cm^{-1}$ reflected the proportion of double helix within total LSA. The red in the scale denoted the highest amount while the blue represented the lowest. The results demonstrated that two conformations of LSA existed in both controls and complexes. In all complexes, it was observed that the intensities of double helical LSA proportion at 856/1343 $cm^{-1}$ decreased with an increase in processing pressure. It can therefore be assumed that the double helical LSA was more susceptible to decomposition when exposed to 600 MPa pressure compared to that of the single helical framework. This result is in agreement with the molecular weight distribution data presented in this paper.

### 3.5. In vitro digestion profiles

Based on *in vitro* digestibility, starch can be classified into RDS, SDS and RS (Englyst et al., 1992). It was suggested that the content RS and SDS are responsible for the anti-digestibility of starchy foods. The amounts of these three components in the samples are shown in Table 2. For LSA controls, the content of RS decreased with increasing processing pressure while the RDS and SDS contents slightly increased. This result agrees with the molecular weight distribution data in this paper, claiming that LSA was degraded into a structure with a lower degree of polymerization and had higher *in vitro* starch digestibility. In previous work, the degradation of LSA under higher hydrostatic pressure lead to a loose and porous arrangement with lower crystallinity (Guo et al., 2018).

Significant enhancement of RS content was observed in the complexes relative to that of LSA controls under both HHP treatments, since the formation of V-type single helical crystals strongly reinforced the ordered and compact structure of the polymeric system (Guo et al., 2018; Zhang et al., 2012). The content of RDS slightly decreased with the formation of complexes while the SDS content decreased significantly, and it can therefore be assumed that SDS tends to be more susceptible to transformation into RS. For both 500 MPa and 600 MPa groups, the RS content increased in the order of LSA-C12:0 > LSA-C14:0 > LSA-C16:0. This result indicates that an increase in RS content is closely related to a decrease in aliphatic chain length of fatty acids, further elucidating a higher crystallinity of the amylose-short chain fatty acid complexes.

Lower RDS values of complexes were observed at 500 MPa than at 600 MPa, indicating lower digestibility of 500 MPa-prepared complexes. The single-helical amylose-fatty acid and double-helical retrograded amylose were defined as RS5 and resistant starch type-3 (RS3), respectively (Dupuis et al., 2014), both of which contribute to the anti-digestibility of the LSA-fatty acid matrix due to the molecular re-arrangement of crystalline. The decomposition effect of single-helical LSA-fatty acid complexes and double-helical retrograded LSA at 600 MPa contributed to a more rapid digestible LSA fragment with a lower degree of polymerization than at 500 MPa, leading to an increase in RDS content.

The hydrolysis properties of LSA-fatty acid complexes are explored and shown in Fig. 4. The results demonstrated that during the first 20 min digestion, samples treated with the same pressure exhibited similar rapid hydrolysis patterns due to the easily digestible RDS. The hydrolysis curves of complexes after 20 min incubation were much lower than those of corresponding LSA controls. HHP could intensify the interactions between LSA and fatty acids through hydrophobic interactions, leading to the formation of slow digestible RS5 crystals (Guo et al., 2018), while the LSA controls with a large proportion of amorphous structure are more vulnerable to enzymes. For both 500 MPa and

**Table 2**
*In vitro* digestibility of complexes prepared by lotus seed amylose and fatty acids with different chain length.[a]

| | Sample[b] | RDS (%) | SDS (%) | RS (%) |
|---|---|---|---|---|
| 500 MPa | LSA | 56.7 ± 2.6a | 26.0 ± 1.3a | 17.3 ± 3.9b |
| | LSA-C12:0 | 54.1 ± 1.3a | 15.6 ± 0.8c | 30.3 ± 0.5a |
| | LSA-C14:0 | 53.3 ± 2.8a | 18.2 ± 1.9bc | 28.6 ± 0.9a |
| | LSA-C16:0 | 55.9 ± 2.1a | 21.7 ± 1.7 ab | 22.4 ± 0.4 ab |
| 600 MPa | LSA | 59.7 ± 1.6a | 27.1 ± 1.8a | 13.2 ± 0.2b |
| | LSA-C12:0 | 58.1 ± 2.3a | 15.0 ± 1.2b | 26.9 ± 1.1a |
| | LSA-C14:0 | 59.3 ± 2.2a | 16.4 ± 0.9b | 24.3 ± 3.1a |
| | LSA-C16:0 | 57.9 ± 3.1a | 17.9 ± 0.2b | 24.2 ± 3.3a |

[a] Data are the averages of three determinations. Values with superscript letters (different samples from the same HHP treatment) within a column are significantly different ($P < 0.05$).

[b] The abbreviations LSA, LSA-C12:0, LSA-C14:0, and LSA-C16:0 represent lotus seed amylose, lotus seed amylose–lauric acid, lotus seed amylose–myristic acid, and lotus seed amylose–palmitic acid, respectively.

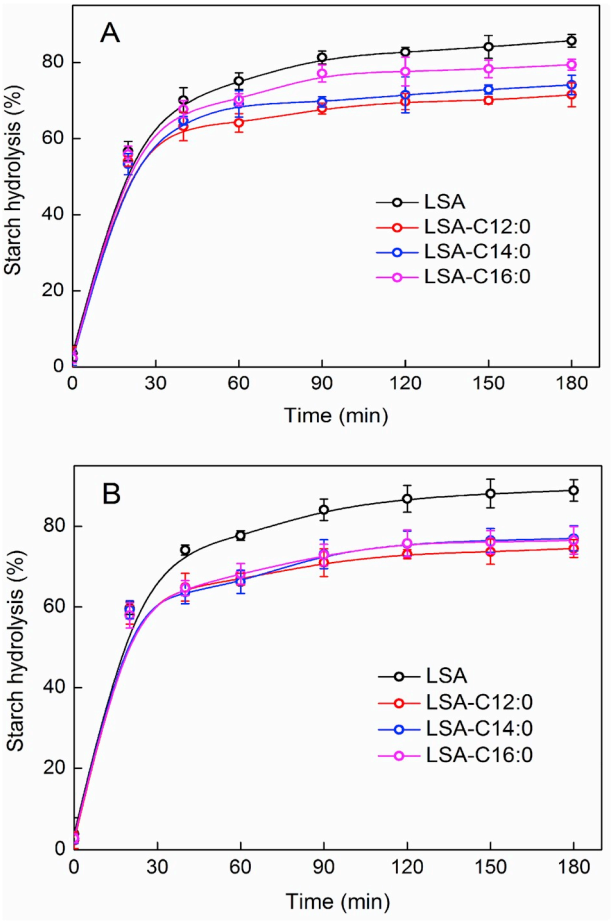


**Fig. 4.** Hydrolysis rate curve of samples prepared under different HHPs (A: 500 MPa; B: 600 MPa). The abbreviations LSA, LSA-C12:0, LSA-C14:0, and LSA-C16:0 represent lotus seed amylose, lotus seed amylose–lauric acid, lotus seed amylose–myristic acid, and lotus seed amylose–palmitic acid, respectively.

600 MPa treatments, LSA-C12:0 showed the lowest hydrolysis curve, indicating the highest proportion of RS content. This result agrees with the CI values and Raman spectra data presented in this paper.

## 4. Conclusion

The HHP treatment resulted in the formation of LSA-fatty acid complexes. The complex of LSA-C12:0 exhibited the highest CI value because of the relatively high dispersivity and low steric hindrance of lauric acid. The morphology of LSA-fatty acid complexes was determined from CLSM and SEM images. The values of *Mw*, *Mn*, polydispersity and resistant starch content of LSA increased with the formation of LSA-fatty acid complexes. An increase in processing pressure from 500 MPa to 600 MPa lead to a decrease in *Mw* and *Mn* values of LSA and complexes due to the decomposition of LSA. The results from Raman spectra and *in vitro* digestion showed that the content of both single helical LSA-fatty acid complex and double helical retrograded LSA are responsible for the digestibility of the matrix. This work provides an in-depth study into the relationship between structure and digestibility of LSA-fatty acid complexes.

## Acknowledgment

The authors gratefully acknowledge the financial support from the National Natural Science Foundation of China (31501485), the FAFU Funds for Distinguished Young Scientists (xjq201618), and the Foundation of International Cooperation and Exchanges in Science and Technology of Fujian Agriculture and Forestry University (grant number KXGH17001).

## Transparency document

Transparency document related to this article can be found online at https://doi.org/10.1016/j.fct.2019.03.052.

## References

Annor, G.A., Marcone, M., Corredig, M., Bertoft, E., Seetharaman, K., 2015. Effects of the amount and type of fatty acids present in millets on their in vitro starch digestibility and expected glycemic index (eGI). J. Cereal Sci. 64, 76–81. https://doi.org/10.1016/j.jcs.2015.05.004.

Birt, D.F., Boylston, T., Hendrich, S., Jane, J.L., Hollis, J., Li, L., McClelland, J., Moore, S., Phillips, G.J., Rowling, M., Schalinske, K., Scott, M.P., Whitley, E.M., 2013. Resistant starch: promise for improving human Health. Adv. Nutr. 4, 587–601. https://doi.org/10.3945/an.113.004325.

Cael, J.J., Koenig, J.L., Blackwell, J., 1975. Infrared and Raman spectroscopy of carbohydrates. Part VI: normal coordinate analysis of V-amylose. Biopolymers 14, 1885–1903. https://doi.org/10.1002/bip.1975.360140909.

Cao, Z., Woortman, A.J.J., Rudolf, P., Loos, K., 2015. Facile synthesis and structural characterization of amylose-fatty acid inclusion complexes. Macromol. Biosci. 15, 691–697. https://doi.org/10.1002/mabi.201400464.

Chen, X., He, X.W., Zhang, B., Fu, X., Li, L., Huang, Q., 2018. Structure, physicochemical and in vitro digestion properties of ternary blends containing swollen maize starch, maize oil and zein protein. Food Hydrocolloids 76, 88–95. https://doi.org/10.1016/j.foodhyd.2017.04.025.

Dupuis, J.H., Liu, Q., Yada, R.Y., 2014. Methodologies for increasing the resistant starch content of food starches: a review. Compr. Rev. Food Sci. Food Saf. 13, 1219–1234. https://doi.org/10.1111/1541-4337.12104.

Englyst, H.N., Kingman, S.M., Cummings, J.H., 1992. Classification and measurement of nutritionally important starch fractions. Eur. J. Clin. Nutr. 46, S33–S50. https://doi.org/10.1128/IAI.01649-06.

Englyst, K.N., Englyst, H.N., Hudson, G.J., Cole, T.J., Cummings, J.H., 1999. Rapidly available glucose in foods: an in vitro measurement that reflects the glycemic response. Am. J. Clin. Nutr. 69, 448–454. https://doi.org/10.0000/PMID10075329.

Farooq, A.M., Dhital, S., Li, C., Zhang, B., Huang, Q., 2018. Effects of palm oil on structural and in vitro digestion properties of cooked rice starches. Int. J. Biol. Macromol. 107, 1080–1085. https://doi.org/10.1016/j.ijbiomac.2017.09.089.

Fredrik, T., Marie, W., Ann-Charlotte, E., 2003. formation of amylose-lipid complexes and effects of temperature treatment. Part 2. Fatty acids. Starch - Stärke 55, 138–149. https://doi.org/10.1002/star.200390028.

Galvis, L., Bertinetto, C.G., Holopainen, U., Tamminen, T., Vuorinen, T., 2015. Structural and chemical analysis of native and malted barley kernels by polarized Raman spectroscopy (PRS). J. Cereal Sci. 62, 73–80. https://doi.org/10.1016/j.jcs.2014.12.008.

Galvis, L., Bertinetto, C.G., Putaux, J.L., Montesanti, N., Vuorinen, T., 2016. Crystallite orientation maps in starch granules from polarized Raman spectroscopy (PRS) data. Carbohydr. Polym. 154, 70–76. https://doi.org/10.1016/j.carbpol.2016.08.032.

Gonzalez-Cruz, L., Montanez-Soto, J.L., Conde-Barajas, E., Negrete-Rodriguez, M.D.X., Flores-Morales, A., Bernardino-Nicanor, A., 2018. Spectroscopic, calorimetric and structural analyses of the effects of hydrothermal treatment of rice beans and the extraction solvent on starch characteristics. Int. J. Biol. Macromol. 107, 965–972. https://doi.org/10.1016/j.ijbiomac.2017.09.074.

Guo, Z.B., Jia, X.Z., Miao, S., Chen, B.Y., Lu, X., Zheng, B.D., 2018. Structural and thermal properties of amylose-fatty acid complexes prepared via high hydrostatic pressure. Food Chem. 264, 172–179. https://doi.org/10.1016/j.foodchem.2018.05.032.

Guo, Z.B., Jia, X.Z., Zhao, B.B., Zeng, S.X., Xiao, J.B., Zheng, B.D., 2017. C-type starches and their derivatives: structure and function. Ann. N. Y. Acad. Sci. 1398, 47–61. https://doi.org/10.1111/nyas.13351.

Guo, Z.B., Zeng, S.X., Lu, X., Zhou, M.L., Zheng, M.J., Zheng, B.D., 2015a. Structural and physicochemical properties of lotus seed starch treated with ultra-high pressure. Food Chem. 186, 223–230. https://doi.org/10.1016/j.foodchem.2015.03.069.

Guo, Z.B., Zeng, S.X., Zhang, Y., Lu, X., Tian, Y.T., Zheng, B.D., 2015b. The effects of ultra-high pressure on the structural, rheological and retrogradation properties of lotus seed starch. Food Hydrocolloids 44, 285–291. https://doi.org/10.1016/j.foodhyd.2014.09.014.

Guo, Z., Zhao, B., Chen, L., Zheng, B., 2019. Physicochemical properties and digestion of Lotus seed starch under high-pressure homogenization. Nutrients 11, 371. https://doi.org/10.3390/nu11020371.

Haaj, S.B., Magnin, A., Petrier, C., Boufi, S., 2013. Starch nanoparticles formation via high power ultrasonication. Carbohydr. Polym. 92, 1625–1632. https://doi.org/10.1016/j.carbpol.2012.11.022.

Jia, X., Sun, S., Chen, B., Zheng, B., Guo, Z., 2018. Understanding the crystal structure of lotus seed amylose–long-chain fatty acid complexes prepared by high hydrostatic pressure. Food Res. Int. 111, 334–341. https://doi.org/10.1016/j.foodres.2018.05.053.

Kawai, K., Takato, S., Sasaki, T., Kajiwara, K., 2012. Complex formation, thermal properties, and in-vitro digestibility of gelatinized potato starch-fatty acid mixtures. Food Hydrocolloids 27, 228–234. https://doi.org/10.1016/j.foodhyd.2011.07.003.

Ma, Z., Boye, J.I., 2018. Research advances on structural characterization of resistant starch and its structure-physiological function relationship: a review. Crit. Rev. Food Sci. Nutr. 58, 1059–1083. https://doi.org/10.1080/10408398.2016.1230537.

Marinopoulou, A., Papastergiadis, E., Raphaelides, S.N., Kontominas, M.G., 2016. Morphological characteristics, oxidative stability and enzymic hydrolysis of amylose-fatty acid complexes. Carbohydr. Polym. 141, 106–115. https://doi.org/10.1016/j.carbpol.2015.12.062.

Mutungi, C., Passauer, L., Onyango, C., Jaros, D., Rohm, H., 2012. Debranched cassava starch crystallinity determination by Raman spectroscopy: correlation of features in Raman spectra with X-ray diffraction and 13C CP/MAS NMR spectroscopy. Carbohydr. Polym. 87, 598–606. https://doi.org/10.1016/j.carbpol.2011.08.032.

Oh, I.K., Bae, I.Y., Lee, H.G., 2018. Complexation of high amylose rice starch and hydrocolloid through dry heat treatment: physical property and in vitro starch digestibility. J. Cereal Sci. 79, 341–347. https://doi.org/10.1016/j.jcs.2017.11.017.

Putseys, J.A., Lamberts, L., Delcour, J.A., 2010. Amylose-inclusion complexes: formation, identity and physico-chemical properties. J. Cereal Sci. 51, 238–247. https://doi.org/10.1016/j.jcs.2010.01.011.

Tang, M.C., Copeland, L., 2007. Analysis of complexes between lipids and wheat starch. Carbohydr. Polym. 67, 80–85. https://doi.org/10.1016/j.carbpol.2006.04.016.

Wang, H.W., Liu, Y.F., Chen, L., Li, X.X., Wang, J., Xie, F.W., 2018. Insights into the multi-scale structure and digestibility of heat-moisture treated rice starch. Food Chem. 242, 323–329. https://doi.org/10.1016/j.foodchem.2017.09.014.

Wang, S., Li, C., Copeland, L., Niu, Q., Wang, S., 2015. Starch retrogradation: a comprehensive review. Compr. Rev. Food Sci. Food Saf. 14, 568–585. https://doi.org/10.1111/1541-4337.12143.

Wellner, N., Georget, D.M.R., Parker, M.L., Morris, V.J., 2011. In situ Raman microscopy of starch granule structures in wild type and ae mutant maize kernels. Starch-Starke 63, 128–138. https://doi.org/10.1002/star.201000107.

Xiang, F.J., Copeland, L., Wang, S., Wang, S.J., 2018. Nature of phase transitions of waxy maize starch in water-ionic liquid mixtures. Int. J. Biol. Macromol. 112, 315–325. https://doi.org/10.1016/j.ijbiomac.2018.01.158.

Yang, Z., Chaib, S., Gu, Q.F., Hemar, Y., 2017. Impact of pressure on physicochemical properties of starch dispersions. Food Hydrocolloids 68, 164–177. https://doi.org/10.1016/j.foodhyd.2016.08.032.

Yoo, S.-H., Jane, J.-l., 2002. Molecular weights and gyration radii of amylopectins determined by high-performance size-exclusion chromatography equipped with multi-angle laser-light scattering and refractive index detectors. Carbohydr. Polym. 49, 307–314. https://doi.org/10.1016/s0144-8617(01)00339-3.

Zabar, S., Lesmes, U., Katz, I., Shimoni, E., Bianco-Peled, H., 2009. Studying different dimensions of amylose-long chain fatty acid complexes: molecular, nano and micro level characteristics. Food Hydrocolloids 23, 1918–1925. https://doi.org/10.1016/j.foodhyd.2009.02.004.

Zabar, S., Lesmes, U., Katz, I., Shimoni, E., Bianco-Peled, H., 2010. Structural characterization of amylose-long chain fatty acid complexes produced via the acidification method. Food Hydrocolloids 24, 347–357. https://doi.org/10.1016/j.foodhyd.2009.10.015.

Zaman, S.A., Sarbini, S.R., 2016. The potential of resistant starch as a prebiotic. Crit. Rev.

Biotechnol. 36, 578–584. https://doi.org/10.3109/07388551.2014.993590.
Zeng, H.L., Chen, P.L., Chen, C.J., Huang, C.C., Lin, S., Zheng, B.D., Zhang, Y., 2018. Structural properties and prebiotic activities of fractionated lotus seed resistant starches. Food Chem. 251, 33–40. https://doi.org/10.1016/j.foodchem.2018.01.057.
Zhang, B., Huang, Q., Luo, F.X., Fu, X., 2012. Structural characterizations and digestibility of debranched high-amylose maize starch complexed with lauric acid. Food Hydrocolloids 28, 174–181. https://doi.org/10.1016/j.foodhyd.2011.12.020.
Zhang, F., Zhang, Y.-Y., Thakur, K., Zhang, J.-G., Wei, Z.-J., 2019. Structural and physicochemical characteristics of lycoris starch treated with different physical methods. Food Chem. 275, 8–14. https://doi.org/10.1016/j.foodchem.2018.09.079.
Zhao, B., Sun, S., Lin, H., Chen, L., Qin, S., Wu, W., Zheng, B., Guo, Z., 2018. Physicochemical properties and digestion of the lotus seed starch-green tea polyphenol complex under ultrasound-microwave synergistic interaction. Ultrason. Sonochem. https://doi.org/10.1016/j.ultsonch.2018.11.001.